Boiling crisis due to bubble interactions

Boiling crisis due to bubble interactions

Lenan Zhang[a†], Shuai Gong[b†], Zhengmao Lu[a], Ping Cheng[b*], Evelyn N. Wang[a*]

a. Department of Mechanical Engineering, Massachusetts Institute of Technology, Cambridge, MA 02139, USA

b. School of Mechanical Engineering, Shanghai Jiao Tong University, Shanghai 200240, P. R. China

ABSTRACT

The boiling crisis determines the maximum heat flux for the safe operation of boiling equipment, which is widely used in various applications including power generation, thermal management of electronics and water desalination. Here we present a mechanistic and predictive theory for the boiling crisis, combining the thermo-fluidic interaction between bubbles and the stochastic interaction of nucleation sites. Using Rayleigh and Poisson distributions, we demonstrate that the boiling crisis occurs when the population of isolated nucleation sites reaches the maximum. We identified a dimensionless boiling crisis constant $1/\pi e$, which universally relates the bubble base diameter to the isolated nucleate site density during the saturated pool boiling crisis. This finding is supported by our direct numerical simulation as well as by previous numerical and experimental results. Combining the thermo-fluidic and stochastic interaction, quantitative and simultaneous predictions of the critical heat flux (CHF) and the corresponding wall superheat at the CHF were achieved, which agrees with existing experimental data. Our theory thus offers a new avenue for understanding the boiling crisis, and therefore can serve as a guideline for the future boiling enhancement design.

Key Words: boiling crisis; critical heat flux; bubble; thermo-fluidic interaction; stochastic interaction

* Corresponding authors
E-mail address: pingcheng@sjtu.edu.cn (P. Cheng), enwang@mit.edu (E.N. Wang)
† Equal contribution to this work

Nomenclature

A	Area (m^2)		
D_b	bubble base diameter (m)	**Greek symbol**	
D_d	bubble departure diameter (m)	θ	contact angle
f	bubble departure frequency (s^{-1})	ρ_v	vapor density (Kg/m^3)
$f(s)$	probability density function	σ	surface tension (N/m)
h_{fg}	specific latent heat (J/Kg)		
n_{iso}	isolated nucleation site density (m^{-2})		
n^*_{iso}	peak of the isolated nucleation density (m^{-2})		
N	number of nucleation site		
N_0	number of intrinsic nucleation site		
P	probability		
q''	heat flux (W/m^2)		
s	nearest neighbor distance (m)		
T_s	saturation temperature (K)		
T_w	wall temperature		
ΔT	superheat (K)		
V	bubble volume (m^3)		

1. Introduction

Boiling is a ubiquitous phenomenon in nature and in industrial processes including power generation, desalination, and ultra-high heat flux electronic cooling [1-3]. This process is typically characterized by the periodic generation of bubbles [4] through liquid-to-vapor phase change on a heated solid surface with thermo-fluidic coupling. The boiling crisis inevitably occurs when the

critical heat flux (CHF) is reached, which is associated with a sudden loss of liquid contact with the heated surface, resulting in a rapid degradation of heat transfer performance and even burnout of devices [1]. Over the past several decades, the boiling crisis has been one of the most elusive fundamental problems in thermal science [5-19]. Traditionally, it has been interpreted as a macroscale thermo-hydrodynamic phenomenon in the hydrodynamic instability model [6] and macrolayer dryout model [7]. Some other studies attributed the trigger of the boiling crisis to the microscale near-wall interfacial phenomena [9, 10, 17]. However, most of these approaches only focused on the heat transfer and fluid mechanics within one vapor bubble/column while neglecting the strong stochastic interaction between neighboring bubbles. More recent experiments by Lloveras *et al*. [12] and Zhang *et al.* [15] demonstrated that the boiling crisis has a percolative nature, implying the significance of stochastic interaction. However, the detailed underlying physical process still remains not well-understood, and a quantitative prediction of the CHF and the associated wall superheat is still lacking. In this work, we show that the boiling crisis can be understood and predicted by combining thermo-fluidic and stochastic interactions between bubbles.

2. Methods

We first describe several key phenomena in the high superheat nucleate boiling regime close to the boiling crisis which have been observed in previous studies [9, 10, 20-22], and then propose a theoretical framework accounting for each individual phenomenon with a statistical model. Figure 1 shows schematics describing the physical process of bubble interactions at low wall superheats and high wall superheats. In the low wall superheat regime, the density of nucleation sites is low. Accordingly, bubble growth and departure are primarily determined by the thermo-fluidic interaction (Fig. 1(a)). However, with the increase of wall superheat, more cavities are thermally activated, inducing stronger thermo-fluidic as well as stochastic interactions (Fig. 1(b)). In particular, prior to departure, a bubble can interact with its neighbors through the competition for bubble base area due to the high activated cavity density ((1) in Fig. 1(b)). In addition, the lateral force arising from the rapid growth of the neighboring bubbles can lead to an early bubble departure with a relatively small bubble diameter D_d ((2) in Fig. 1(b)). This phenomenon was experimentally observed by Gaertner and Westwater [23] and theoretically described by Kolev [20] (Section I of Supplemental Material for a brief introduction of Kolev's model). It is also worth

mentioning that the vapor recoil effect driven by the strong interfacial mass flux at the three-phase contact line leads to the increase of bubble apparent contact angle θ_a ((3) in Fig. 1(b)) [10, 22]. This effect is accounted for by assuming $\theta_a = 90^o$ when the bubble intrinsic contact angle $\theta \leqslant 90^o$ and $\theta_a = \theta$ when $\theta > 90^o$. When $\theta_a \geqslant 90^o$, a small residual bubble will be left on the heating surface when the bubble departs and the waiting period in the ebullition cycle disappears [21, 22, 24] ((4) in Fig. 1(b)). If the distance between two adjacent nucleation sites is smaller than the bubble base diameter D_b, they will interact ((5) of Fig. 1(b)). This interaction stochastically occurs due to the random distribution of nucleation sites. The coalescence of the hot spot under the bubble base causes the formation of an unrewettable dry area and reduces the number of active nucleation sites ((5) in Fig. 1(b)). The isolated nucleation sites (N_{iso}) account for most of the heat transfer at the boiling crisis whereas the unrewettable dry area has little contribution. Fig. 1(c) (1)-(5) shows schematically the detailed process, which was confirmed by previous studies [9, 10, 20-22].

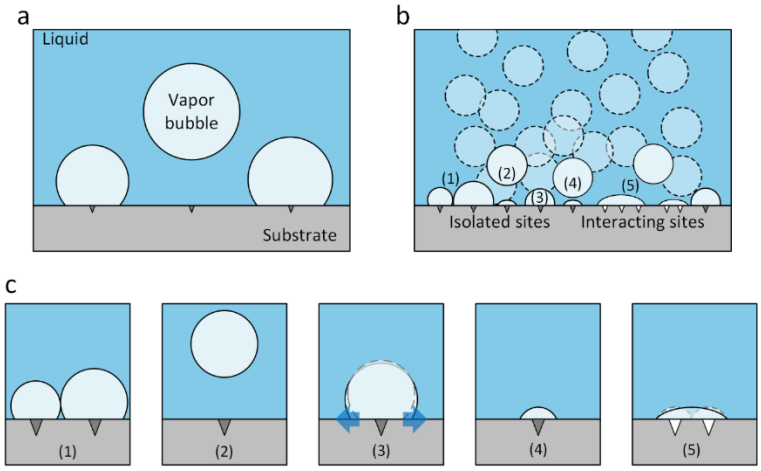

FIG. 1. Schematic describing bubble interactions: (a) at low wall superheat regime where the bubble interaction is weak due to the low nucleation site density, and therefore the nucleation sites are isolated (marked as grey triangles), and (b) at high wall superheat regime, where strong coupling of the thermo-fluidic and stochastic interaction occurs (with interacting sites marked by white triangles). (c) Details of processes which lead to (1) neighboring bubble interaction, (2) early departure of the bubble with a smaller bubble departure size, (3) increase of the apparent contact angle, (4) small residual bubble covering the nucleation sites, and (5) formation of unrewettable dry area due to the interaction of neighboring nucleation sites.

To describe the stochastic nature of nucleation, which governs processes (4) and (5) in Fig. 1(c), we consider the probability P of finding N intrinsic sites on a heated surface with a finite area A, where the intrinsic sites are the thermally activated cavities determined by cavity size distributions, superheat and the wettability of the heated surface [25, 26]. As demonstrated in our recent experimental findings and theoretical analysis [27], N follows a two-dimensional Poisson process (see Section II of Supplemental Material for derivation),

$$P(N, N_0) = \frac{N_0^N}{N!} e^{-N_0} \tag{1}$$

where N_0 is the expected number of intrinsic nucleation sites which is related to the intrinsic nucleation site density n_0 by $n_0 = N_0/A$. Since the stochastic interaction of nucleation sites originates from the random spatial distribution of intrinsic sites, the distribution of the nearest neighbor distance between intrinsic sites s should also be investigated. Many previous studies suggested that s follows a Poisson distribution [26]. However, the distribution of s should be a continuous probability density function while the Poisson distribution is discrete by nature. To address this inconsistency, we theoretically derived the distribution function of s. Instead of a Poisson process, we show that s obeys the following Rayleigh distribution [27],

$$f(s) = \frac{s}{\sigma^2} e^{-\frac{s^2}{2\sigma^2}} \tag{2}$$

where $f(s)$ is the probability density function and $\sigma^2 = A/2\pi N$ (Section III of Supplemental Material for detailed derivations). Combining the Poisson and Rayleigh distributions, the average number of isolated nucleation sites is given by (Section IV of Supplemental Material for detailed derivations),

$$N_{iso} = \sum_{N=1}^{\infty} \frac{N_0^N}{(N-1)!} e^{-\left(N_0 + \frac{\pi N D_b^2}{A}\right)} \tag{3}$$

where the average number density of isolated nucleation sites is thus $n_{iso} = N_{iso}/A$.

3. Results and discussion

Figure 2 shows the behavior of intrinsic and isolated nucleation site density as a function of wall superheat ΔT at three representative D_b, where we used the experimentally characterized

temperature and wettability dependent $n_0(\Delta T)$ from Wang and Dhir [26] (indicated as dashed lines in Figs. 2(a) and (b)), which is given as: $n_0(\Delta T)\ \text{sites/cm}^2 = 5 \times 10^5\ (1-\cos\theta) \times (2r_c)^{-6}$, with r_c being the critical nucleation radius defined by $r_c = 2\sigma \cdot T_s/\left[\rho_v \cdot h_{fg} \cdot (T_w - T_s)\right]$. Note that to elucidate the stochastic nature of bubble interaction, we treated the bubble base D_b as a parameter in Fig. 2. However, in the prediction of CHF which will be shown later, D_b in the high superheat nucleate boiling regime is rigorously determined by Gaertner and Westwater's [23] experiment and Kolev's [20] theory. As expected, n_{iso} firstly increases with ΔT, reaches a peak value n^*_{iso} and then decreases due to the strong stochastic interaction, showing a similar profile to the classical Nukiyama pool boiling curve [28]. Therefore, we expect the boiling crisis to be a state when n_{iso} reaches a maximum, and the ΔT corresponding to n^*_{iso} is the wall superheat at CHF (ΔT_{CHF}). Note that n_{iso} finally approaches zero at a sufficiently high ΔT, indicating that all intrinsic sites interact with their neighbors, where a vapor film on the heating surface is formed.

Under this theoretical approach, we anticipate that the boiling process is characterized by several dimensionless constants, independent of operating conditions. Specifically, pool boiling near CHF can be characterized with a dynamic similarity, which is defined by a dimensionless constant $\Pi = n^*_{iso} \times D_b^2 = 1/(\pi e) \approx 0.117$ (Section IV of Supplemental Material for detailed analysis). Due to this dynamic similarity, n^*_{iso} is independent of the surface wettability for a given D_b (Fig. 2(b)). However, the corresponding ΔT at n^*_{iso} is still a function of wettability since nucleation becomes more difficult for more hydrophilic surfaces. In addition, we theoretically show that n^*_{iso} always accounts for approximately 37% of n_0 at the boiling crisis (Section IV of Supplemental Material for details). Consequently, $\Pi = 1/(\pi e)$ provides a range of the dry area fraction at CHF, where the lower bound is determined by the coverage of all isolated sites, *i.e.*, $n^*_{iso} \times \pi D_b^2/4 = 9.2\%$ area of the total heating surface while the upper bound is given by $n_0 \times \pi D_b^2/4 = 25\%$. To validate this theoretically predicted range (blue band in Fig. 2(c)), we compare the dry area fraction obtained by various simulations and experiments and show good agreement. Specifically, we perform direct numerical simulation of pool boiling using the lattice Boltzmann method (LBM), which shows that the average dry area fraction (blue circles in Fig. 2(c)) is about 23% at CHF (See Appendix A for simulation details). Similar dry area fractions at CHF were observed in Jung *et al.*'s [29] experiment (18%) and Sato and Niceno's [30] simulation (24%) using an interface tracking approach (blue circles in Fig. 2(c)). More interestingly, the isolated site area fraction at CHF

(orange squares in Fig. 2(c)) given by existing simulation (9.7%) [30] and experimental data (8.6%) [23] matches well with the theoretically predicted value (9.2%, orange-dashed line in Fig. 2(c)), suggesting that $\Pi = 1/(\pi e)$ is a fundamental boiling crisis constant.

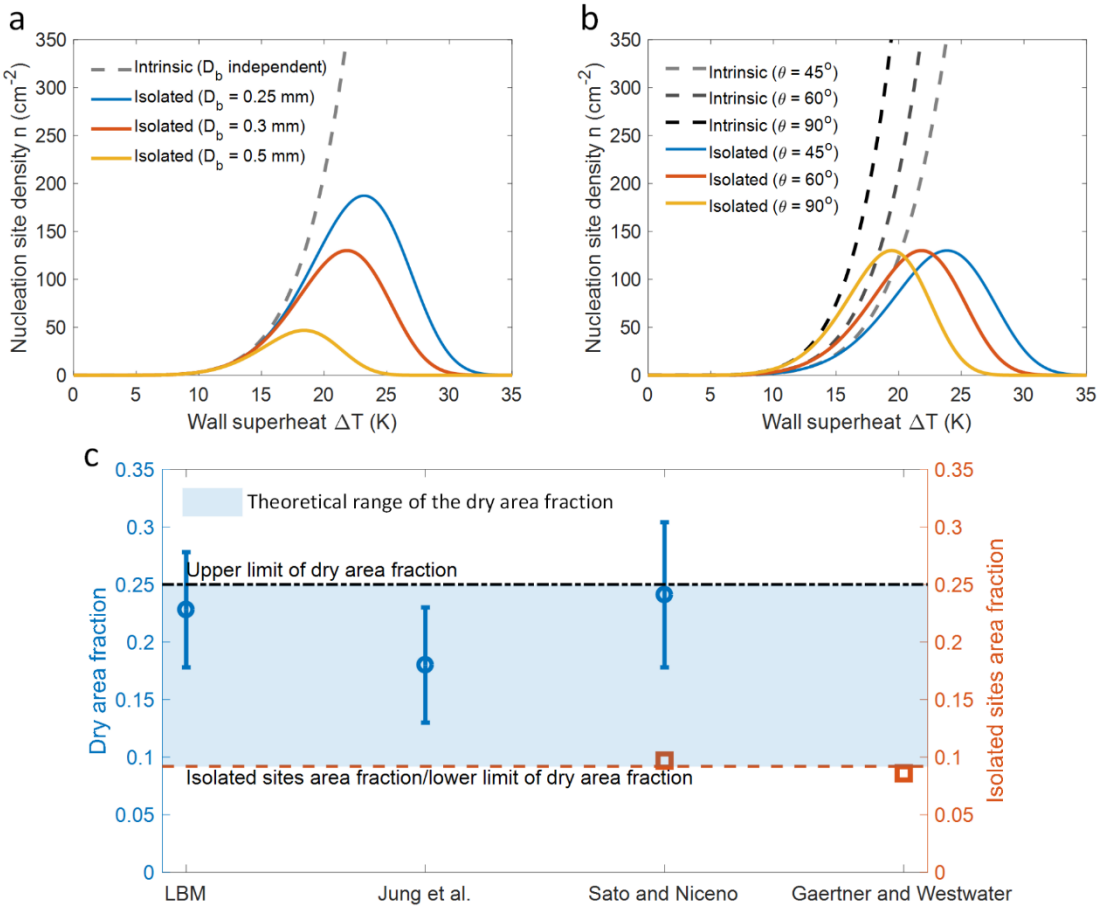

FIG. 2. Stochastic interaction of nucleation sites and the resulting dry area fraction based on Poisson and Rayleigh distributions. Isolated site density n_{iso} as a function of wall superheat ΔT at three representative (a) bubble base diameters D_b when $\theta = 60^o$ and (b) contact angles θ when $D_b = 0.3$ mm. n_{iso} has a peak value n^*_{iso} due to the stochastic interaction which is characterized by a dimensionless constant $\Pi = n^*_{iso} \times D_b^2 = 1/(\pi e)$. (c) Comparison between the theoretically predicted dry area fraction and various simulation and experimental data. The upper and lower bounds of the dry area fraction are 25% and 9.2% which are determined by $n_0 \times \pi D_b^2/4$ and $n^*_{iso} \times \pi D_b^2/4$ at CHF, respectively. The blue band indicates the theoretical range of the dry area fraction. Good agreement is shown between theory and experiments. The uncertainty of the LBM simulation is determined by the standard deviation due to the temporal fluctuation of dry area fraction. The

orange-dashed line indicates the theoretically predicted isolated sites area fraction at CHF, and the orange squares represent the numerically simulated (Sato and Niceno [30]) and experimentally characterized isolated sites area fraction at CHF (Gaertner and Westwater [23]).

To elucidate the connection between the stochastic interaction and the percolative nature of the boiling crisis, we define the nucleation site interaction probability as $P_{inter} = 1\text{-}N_{iso}/N_0$, which is plotted as a function of wall superheat for select D_b and θ in Figs. 3(a) and (b), respectively. We can observe a sudden change in P_{inter} when ΔT becomes large enough, which is triggered at a lower wall superheat for larger D_b or θ. In fact, as the intrinsic sites follow a 2D spatial Poisson process, this sudden change can be interpreted by the Boolean-Poisson model [31] using the continuum percolation theory which describes the interaction of Gilbert disks centered at different random points following a Poisson process [32]. In the boiling scenario, the random points are intrinsic nucleation sites and the Gilbert disk represents the bubble base with diameter D_b. According to percolation theory, we can predict the percolation threshold $\eta_c = \pi D_b^2 n_0/4 \approx 1.128$ [33] where most of bubble base regions are interconnected. At this percolation threshold, we found that more than 98% of total intrinsic nucleation sites interact with their neighbors (dashed line in Figs. 3(a) and (b)). For this reason, the percolation threshold ($\eta_c \approx 1.128$) is another characteristic point for the boiling process, indicating the transition to film boiling.

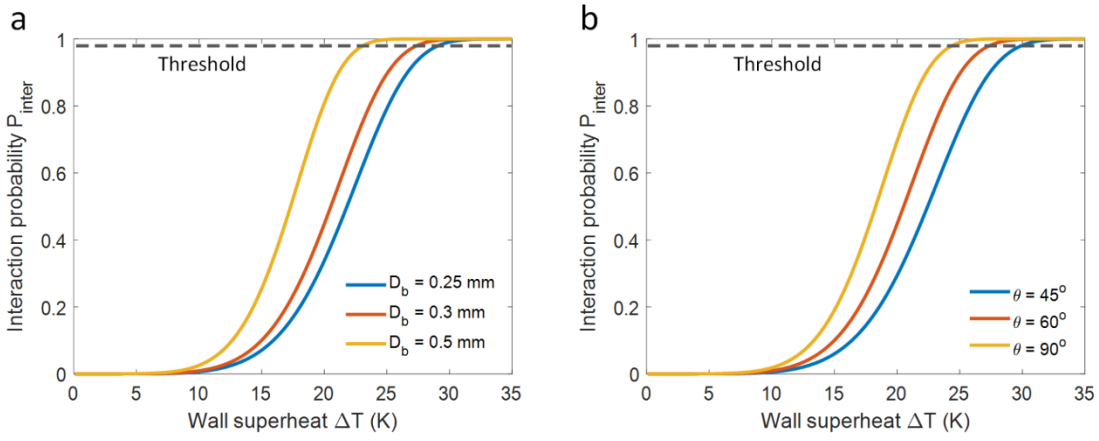

FIG. 3. Interaction probability P_{int} as a function of wall superheat ΔT at three representative (a) bubble base diameters D_b when $\theta = 60^o$ and (b) contact angles θ when $D_b = 0.3$ mm. The sudden change in P_{int} can be understood by the Boolean-Poisson model in the continuum percolation

theory due to the spatial 2D Poisson process of intrinsic sites. A dimensionless constant $\eta_c = \pi D_b^2 n_0/4 \approx 1.128$ due to the percolation threshold indicates transition to film boiling.

To quantitatively predict CHF and the corresponding ΔT_{CHF}, we combined the thermo-fluidic and stochastic interactions (effects (1)-(5) in Fig. 1). Based on the energy balance, CHF can be expressed as (See Appendix B for the justification),

$$CHF = h_{fg}\rho_v V n_{iso}^* f \tag{4}$$

where h_{fg}, ρ_v, V and f are the vaporization enthalpy of fluid, density of vapor, single bubble volume and bubble departure frequency, respectively. Note that V and f are determined by the bubble departure diameter and bubble growth shown in Eqs. (S1-S3) in Section I of Supplemental Material. Therefore, the calculation of CHF using Eq. (4) considered both the thermo-fluidic interaction which determines the bubble diameter, bubble volume and bubble frequency, and stochastic interaction which determines the isolated nucleation site density (See Appendix C for details).

Figure 4 shows that the predicted CHF and the corresponding ΔT_{CHF} decreases with θ based on the proposed theory. The theoretical predictions were compared with experimental data [21, 26, 34-38] for water under 1 atm, showing good agreement. Predictions from Zuber [6]'s and Kandlikar [8]'s models are also shown for comparison (Fig. 4(a)). Note that we showed two bubble diameters in Fig. 4 because both experimental results [23] and theoretical predictions [20] indicate that bubble departure size ranges from 0.25 mm to 0.3 mm in the high superheat nucleate boiling regime to CHF. Since θ does not affect n^*_{iso} (Fig. 2(b)), the decrease of CHF with θ shown in Fig. 4(a) arises from the decrease of bubble departure frequency with increasing θ. The kink in the predicted CHF curve at 90° (Fig. 4(a)) is attributed to the treatment of the vapor recoil effect. On the other hand, ΔT_{CHF} decreases with θ (Fig. 4(b)) because less cavities can be thermally activated on a more hydrophilic surface (Fig. 2(b)). In particular, the theoretical prediction of ΔT_{CHF} agrees well with both the experimental results of Dhir and Liaw [34] and Wang and Dhir [26] using the expression of n_0 suggested by Wang and Dhir [26] (Fig. 4(b)). Since ΔT_{CHF} is determined by the peak value of Eq. (3), the good agreement shown in Fig. 4(b) further supports our hypothesis that boiling crisis occurs when n_{iso} reaches a maximum. To further demonstrate the applicability of the proposed CHF model, we also calculated the CHF of FC-72 using our theory and the predicted CHF of 13.3 W/cm^2 agrees well with the experimental result of 12.7 W/cm^2 [39]. Based on the

nucleation site density at CHF reported by Zhang *et al.* [15], we back calculated the CHF using our theory and found that the predicted CHF of 90 W/cm^2 was also in reasonable agreement with their experimental result of 117 W/cm^2, where the discrepancy can be originated from the uncertainties in the characterization of nucleation site density.

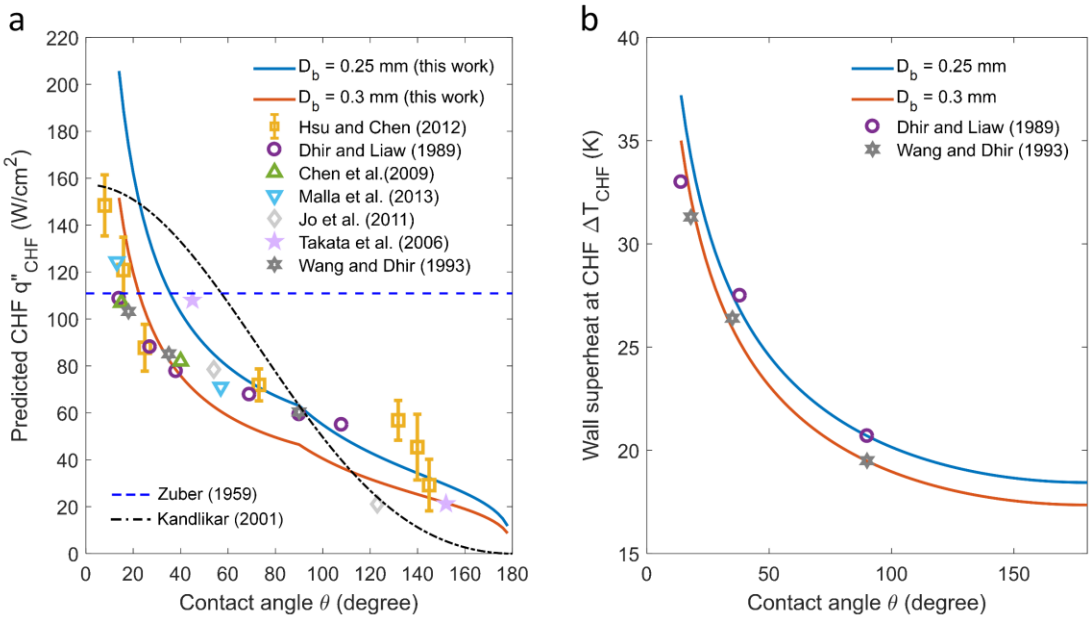

FIG. 4. Comparison of the predicted (a) CHF and (b) ΔT_{CHF} as a function of surface wettability with existing experimental data. $D_b \approx 0.25$-0.3 mm, which shows reasonably good agreement.

4. Concluding remarks

In summary, we developed a bubble interaction model framework to understand and predict the boiling crisis. We showed that the physical origin of the boiling crisis is the coupling of thermo-fluidic and stochastic interaction. To describe the stochastic interaction of nucleation sites, we applied Poisson and Rayleigh distributions for the population and spatial distribution of intrinsic nucleation sites, respectively. The boiling crisis occurs when the number of isolated nucleation sites reaches a maximum. In particular, we found that two dimensionless constants characterize boiling phenomena where $\Pi = n^*_{iso} \times D_b^2 = 1/(\pi e)$ corresponds to the boiling crisis and $\eta_c = \pi D_b^2 n_0/4 \approx 1.128$ represents the transition to film boiling. Combining the thermo-fluidic and stochastic interaction, quantitative predictions of CHF and the corresponding ΔT_{CHF} were achieved, which agrees with existing experimental data. Results of this work could guide future CHF enhancement

design, which is crucial for the safe operation and efficiency of various boiling systems, including for thermal management of electronics, power generation, and water desalination.

We thank X. Li, L. Zhao, R. Iwata, and Y. Song for insightful discussions. We also would like to thank Dr. Yohei Sato for providing the simulation results for comparison. S. Gong acknowledges the support from National Natural Science Foundation of China (No. 51706135), National Science and Technology Major Project (No. 2018ZX06002004), Shanghai Pujiang Program (No. 20PJ1406800), and Foundation for Innovative Research Groups of National Natural Science Foundation of China (No. 51521004). This paper is based upon work supported by the Singapore-MIT Alliance for Research and Technology (SMART) LEES Program.

Appendix A: Direct numerical simulation of pool boiling process using LBM

To obtain the dry area fraction at CHF point and support our CHF theory, we conduct direct numerical simulations of pool boiling process by the lattice Boltzmann method (LBM). Details of the model can be found from our previous work [22, 40]. The simulated boiling curve using this approach showed the same features with the classical Nukiyama boiling curve [28]. In particular, the CHF predicted by our simulation [22, 40] agrees well with classical model [6]. The heat transfer in the film boiling regime predicted by our LBM simulation also agreed well with the Berenson's classical solution [41].

Figure A1 shows the simulated 3D saturated pool boiling patterns of CHF point at two typical instants. The time-averaged dry area fraction during a sufficiently long-time interval at CHF point is determined to be 23±5% where the uncertainty is the standard deviation of the dry area fraction.

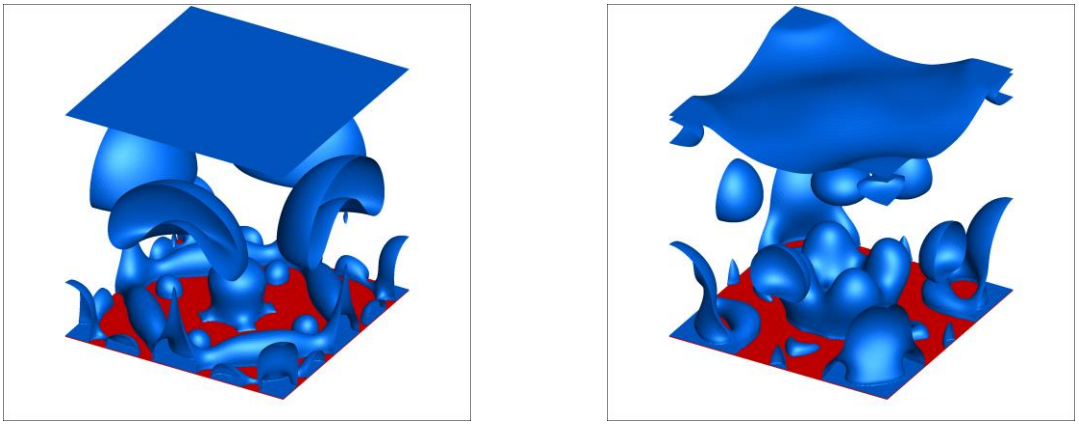

FIG. A1. Representative LBM simulated pool boiling patterns at CHF point (Red: heater; Blue: vapor bubble).

Appendix B: Energy balance analysis during the pool boiling process

In this Section, we perform an energy balance analysis to justify Eq. (4) in the main text, which states that most of the heat is carried by the liquid-to-vapor phase change during saturated pool boiling. Fig. A2 shows the schematic of a typical pool boiling experimental setup, where the sidewall is thermally insulated, and a reflux condenser is used to return condensed liquid to the liquid pool. We define the entire liquid pool as the control volume (marked as the dashed box in Fig. A2). At a steady state, the total vapor mass flow rate $\dot{m}_v$ leaving the control volume is equal to the mass flow rate of the condensed liquid $\dot{m}_l$ returning to the control volume, *i.e.*, $\dot{m}_v = \dot{m}_l$, where $\dot{m}_v$ consists of the vapor flow carried by bubbles $\dot{m}_{bub}$ and direct evaporation at the liquid-vapor interface $\dot{m}_{evap}$. Note the contribution of $\dot{m}_{evap}$ is negligible since both the liquid-vapor interface and vapor above the interface are in the saturated state, and the pressure or concentration gradient which drives the direct evaporation is insignificant. Considering the sidewall has good thermal insulation, the energy balance of the control volume is given by,

$$\dot{Q} = \dot{m}_v h_{fg} + \dot{m}_l c_{p,l}(T_{sat} - T_l) \approx \dot{m}_{bub} h_{fg} + \dot{m}_{bub} c_{p,l}(T_{sat} - T_l) \quad \text{(A1)}$$

where $\dot{Q}$ is the total heat transfer rate input from the heating substrate and T_l is the temperature of condensed liquid. Since h_{fg} (~10^6 J/kg) is one to two orders of magnitude larger than $c_{p,l}(T_{sat} - T_l)$ (~10^4-10^5 J/kg), most of heat transfer during the saturated pool boiling is carried by the vapor flow due to bubble generation. On the other hand, since most of vapor bubbles are generated on the bottom solid-fluid interface through heterogeneous nucleation, $\dot{m}_{bub}$ is determined by the liquid-to-vapor phase change on the heating surface,

$$\dot{m}_{bub} = \rho_v V N_{act} f \quad \text{(A2)}$$

where V is the bubble volume and N_{act} is the average number of the active nucleation sites. At CHF, we assumed $N_{act} \approx N_{iso}$, since the interacting nucleation sites form large unrewettable area which provides little heat transfer. Combining Eqs. (A1) and (A2), we obtain Eq. (4) in the main text,

$$CHF = h_{fg}\rho_v V n^*_{iso} f. \quad \text{(A3)}$$

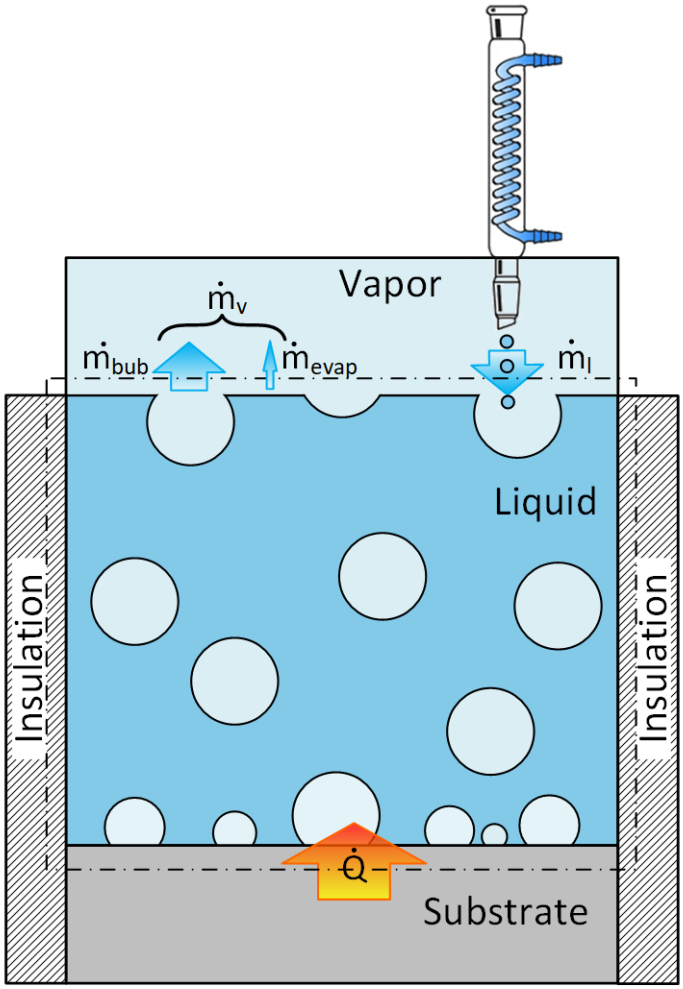

FIG. A2. Schematic of the heat and mass transport in a typical saturated pool boiling experimental setup. The entire liquid pool (the dashed box) is chosen as the control volume for mass and energy balance analysis. Heat flows into the control volume from the bottom heating substrate and vapor flows out from the top liquid-vapor interface. Condensed liquid returns to the control volume from a reflux condenser. The sidewall of the liquid pool is thermally insulated.

Appendix C: Descriptions of the modeling framework

Figure A3 shows the modeling framework developed in this work which combines the thermo-fluidic interaction with the stochastic interaction. The only input parameters are fluid properties (*e.g.*, vaporization enthalpy, density, viscosity, thermal conductivity, and thermal diffusivity, *etc.*) and the intrinsic nucleation site density correlation/model for n_0 (grey block in Fig. A3), which is determined by the property of heating surfaces. In this work, we chose the intrinsic nucleation site density correlation developed by Wang and Dhir [26], which is commonly used to describe the nucleation on metallic surfaces (*e.g.*, copper).

As described in the main text and Section I, the thermo-fluidic interaction determines the bubble growth and departure (yellow blocks in Fig. A3), where the bubble growth is described by the classical diffuse-controlled growth process (Eqs. (S1) to (S3)), and the fluidic forces induced bubble departure is modeled by Eqs. (S4) to (S8) according to Kolev's theory [20]. The bubble volume V is calculated by the departure diameter D_d, and the bubble departure frequency f is given by Eq. (S7) by substituting D_d into the diffuse-controlled growth model (Eq. (S1)).

On the other hand, the stochastic interaction arises from the random distribution of bubble population and nearest neighbor distance (blue blocks in Fig. A3). As shown in the main text and Sections II and III of this Supplemental Material, the population of nucleation sites follows the Poisson distribution (Eq. (1) and Eqs. (S9) to (S16)), and the nearest neighbor distance is described by the Rayleigh distribution (Eq. (2) and Eqs. (S17) to (S21)). Combining the population and nearest neighbor distance distributions, the active nucleation site density can be therefore determined with the bubble base diameter D_b as an input parameter (green block in Fig. A3), which is given by the thermo-fluidic interaction model (Eq. (3) and Eqs. (S22) to (S25)). Finally, we predicted CHF using the energy balance relationship (Eq. (4)) with bubble volume V, bubble departure frequency f, and peak of the isolated nucleation site density n^*_{iso} as input parameters (purple block in Fig. A3).

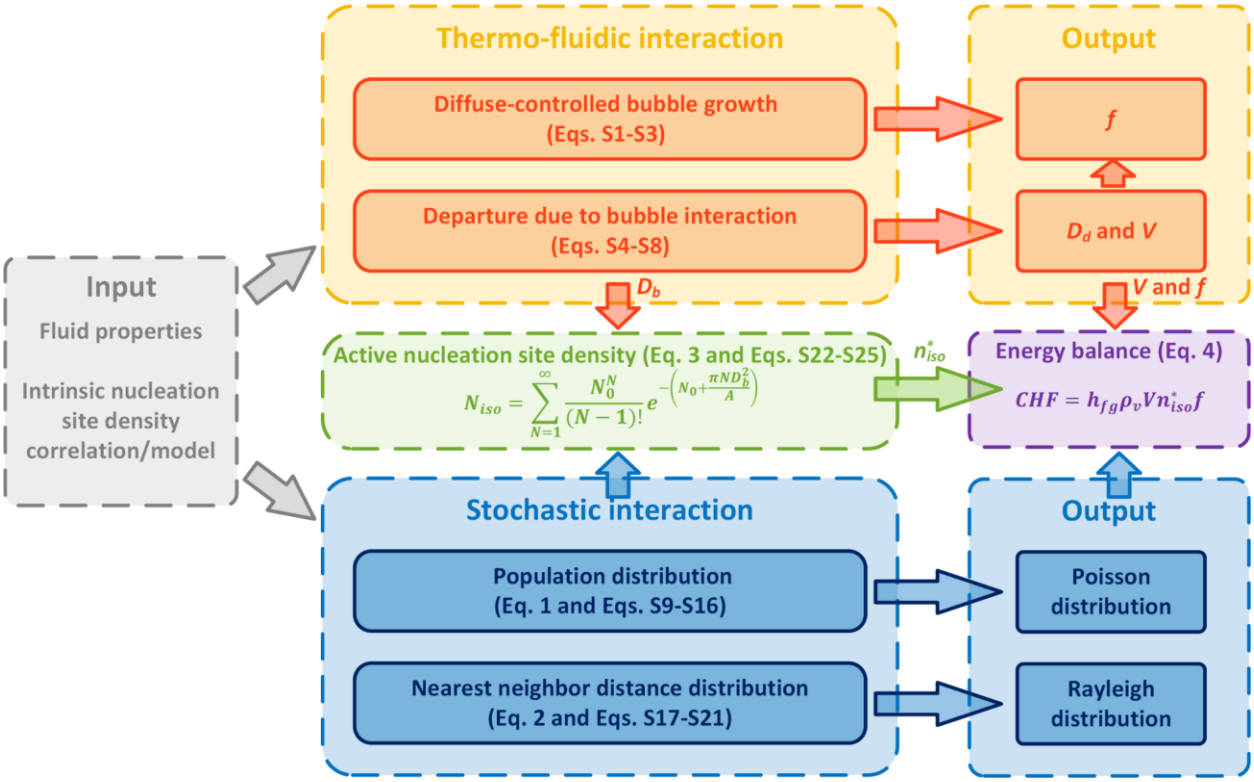

FIG. A3. Modeling framework for the boiling crisis combining the thermo-fluidic interaction and stochastic interaction. Grey block: input parameters including fluid properties and the intrinsic nucleation site density correlation/model. Yellow blocks: thermo-fluidic interaction model which considers the diffuse-controlled bubble growth due to heat transport and early departure of bubble due to fluid dynamic forces. Blue blocks: stochastic interaction model which considers the random distribution of nucleation site population and nearest neighbor distance. Green block: active nucleation site density due to the thermo-fluidic and stochastic interactions. Purple block: CHF predicted by the overall energy balance which takes the results of thermo-fluidic and stochastic interactions as inputs.

References

[1] V.P. Carey, Liquid-Vapor Phase-Change Phenomena: An Introduction To The Thermophysics Of Vaporization And Condensation Processes In Heat Transfer Equipment, Taylor & Francis Group, New York, 2008.
[2] H.J. Cho, D.J. Preston, Y. Zhu, E.N. Wang, Nanoengineered materials for liquid–vapour phase-change heat transfer, Nature Reviews Materials, 2(2) (2016) 16092.
[3] Y. Peles, Boiling Heat Transfer Enhancement at the Microscale, in: ENCYCLOPEDIA OF TWO-PHASE HEAT TRANSFER AND FLOW II: SPECIAL TOPICS AND APPLICATIONS, World Scientific, 2016, pp. 109-136.
[4] L. Zhang, S. Gong, Z. Lu, P. Cheng, E.N. Wang, A unified relationship between bubble departure frequency and diameter during saturated nucleate pool boiling, Int J Heat Mass Tran, 165 (2021) 120640.
[5] S. Kutateladze, On the transition to film boiling under natural convection, Kotloturbostroenie, 3 (1948) 10-12.
[6] N. Zuber, Hydrodynamic aspects of boiling heat transfer, PhD Dissertation, University of California, Los Angeles, 1959.
[7] Y. Haramura, Y. Katto, A new hydrodynamic model of critical heat flux, applicable widely to both pool and forced convection boiling on submerged bodies in saturated liquids, Int J Heat Mass Tran, 26(3) (1983) 389-399.
[8] S.G. Kandlikar, A theoretical model to predict pool boiling CHF incorporating effects of contact angle and orientation, J. Heat transfer, 123(6) (2001) 1071-1079.
[9] T. Theofanous, T.-N. Dinh, J. Tu, A. Dinh, The boiling crisis phenomenon: Part II: dryout dynamics and burnout, Experimental Thermal and Fluid Science, 26(6-7) (2002) 793-810.
[10] V. Nikolayev, D. Chatain, Y. Garrabos, D. Beysens, Experimental evidence of the vapor recoil mechanism in the boiling crisis, Physical review letters, 97(18) (2006) 184503.
[11] K.-H. Chu, R. Enright, E.N. Wang, Structured surfaces for enhanced pool boiling heat transfer, Applied Physics Letters, 100(24) (2012) 241603.
[12] P. Lloveras, F. Salvat-Pujol, L. Truskinovsky, E. Vives, Boiling crisis as a critical phenomenon, Physical review letters, 108(21) (2012) 215701.
[13] V.V. Yagov, Is a crisis in pool boiling actually a hydrodynamic phenomenon?, Int J Heat Mass Tran, 73 (2014) 265-273.
[14] N.S. Dhillon, J. Buongiorno, K.K. Varanasi, Critical heat flux maxima during boiling crisis on textured surfaces, Nature communications, 6(1) (2015) 1-12.
[15] L. Zhang, J.H. Seong, M. Bucci, Percolative scale-free behavior in the boiling crisis, Physical review letters, 122(13) (2019) 134501.
[16] Y. Song, L. Zhang, Z. Liu, D.J. Preston, E.N. Wang, Effects of airborne hydrocarbon adsorption on pool boiling heat transfer, Applied Physics Letters, 116(25) (2020) 253702.
[17] D.E. Kim, J. Song, H. Kim, Simultaneous observation of dynamics and thermal evolution of irreversible dry spot at critical heat flux in pool boiling, Int J Heat Mass Tran, 99 (2016) 409-424.
[18] R. Wen, Q. Li, W. Wang, B. Latour, C.H. Li, C. Li, Y.-C. Lee, R. Yang, Enhanced bubble nucleation and liquid rewetting for highly efficient boiling heat transfer on two-level hierarchical surfaces with patterned copper nanowire arrays, Nano Energy, 38 (2017) 59-65.
[19] L.-W. Fan, J.-Q. Li, D.-Y. Li, L. Zhang, Z.-T. Yu, Regulated transient pool boiling of water during quenching on nanostructured surfaces with modified wettability from superhydrophilic to superhydrophobic, Int J Heat Mass Tran, 76 (2014) 81-89.
[20] N.I. Kolev, The influence of mutual bubble interaction on the bubble departure diameter, Experimental thermal and fluid science, 8(2) (1994) 167-174.
[21] H. Jo, H.S. Ahn, S. Kang, M.H. Kim, A study of nucleate boiling heat transfer on hydrophilic, hydrophobic and heterogeneous wetting surfaces, Int J Heat Mass Tran, 54(25-26) (2011) 5643-5652.

[22] S. Gong, L. Zhang, P. Cheng, E.N. Wang, Understanding triggering mechanisms for critical heat flux in pool boiling based on direct numerical simulations, Int J Heat Mass Tran, 163 (2020) 120546.
[23] R.F. Gaertner, J. Westwater, Population of active sites in nucleate boiling heat transfer, Chem. Eng. Progr., 56(30) (1960) 39-48.
[24] S. Dash, L. Rapoport, K.K. Varanasi, Crystallization-Induced Fouling during Boiling: Formation Mechanisms to Mitigation Approaches, Langmuir, 34(3) (2018) 782-788.
[25] P. Griffith, J.D. Wallis, The role of surface conditions in nucleate boiling, Chem. Eng. Prog. Symp. Ser., 56 (1960) 49-62.
[26] C.H. Wang, V.K. Dhir, Effect of Surface Wettability on Active Nucleation Site Density During Pool Boiling of Water on a Vertical Surface, Journal of Heat Transfer, 115(3) (1993) 659-669.
[27] L. Zhang, R. Iwata, L. Zhao, S. Gong, Z. Lu, Z. Xu, Y. Zhong, J. Zhu, S. Cruz, K.L. Wilke, P. Cheng, E.N. Wang, Nucleation Site Distribution Probed by Phase-Enhanced Environmental Scanning Electron Microscopy, Cell Reports Physical Science, 1(12) (2020) 100262.
[28] S. Nukiyama, The maximum and minimum values of the heat Q transmitted from metal to boiling water under atmospheric pressure, Int J Heat Mass Tran, 9(12) (1966) 1419-1433.
[29] J. Jung, S.J. Kim, J. Kim, Observations of the Critical Heat Flux Process During Pool Boiling of FC-72, Journal of Heat Transfer, 136(4) (2014) 041501.
[30] Y. Sato, B. Niceno, Pool boiling simulation using an interface tracking method: From nucleate boiling to film boiling regime through critical heat flux, Int J Heat Mass Tran, 125 (2018) 876-890.
[31] S.N. Chiu, D. Stoyan, W.S. Kendall, J. Mecke, Stochastic geometry and its applications, John Wiley & Sons, 2013.
[32] E.N. Gilbert, Random plane networks, Journal of the society for industrial and applied mathematics, 9(4) (1961) 533-543.
[33] K. Meeks, J. Tencer, M.L. Pantoya, Percolation of binary disk systems: Modeling and theory, Physical Review E, 95(1) (2017) 012118.
[34] V.K. Dhir, S.P. Liaw, Framework for a Unified Model for Nucleate and Transition Pool Boiling, Journal of Heat Transfer, 111(3) (1989) 739-746.
[35] Y. Takata, S. Hidaka, T. Uraguchi, Boiling feature on a super water-repellent surface, Heat Transfer Eng, 27(8) (2006) 25-30.
[36] R. Chen, M.-C. Lu, V. Srinivasan, Z. Wang, H.H. Cho, A. Majumdar, Nanowires for enhanced boiling heat transfer, Nano letters, 9(2) (2009) 548-553.
[37] C.-C. Hsu, P.-H. Chen, Surface wettability effects on critical heat flux of boiling heat transfer using nanoparticle coatings, Int J Heat Mass Tran, 55(13-14) (2012) 3713-3719.
[38] S. Malla, M. Amaya, S. You, Experimental study of pool boiling heat transfer in water from hydrophilic and hydrophobic surfaces, in: Proc. 8th Int. Conf. Multiphase Flow, , Jeju, Korea, 2013.
[39] K.N. Rainey, S.M. You, Effects of heater size and orientation on pool boiling heat transfer from microporous coated surfaces, Int J Heat Mass Tran, 44(14) (2001) 2589-2599.
[40] S. Gong, P. Cheng, Direct numerical simulations of pool boiling curves including heater's thermal responses and the effect of vapor phase's thermal conductivity, Int Commun Heat Mass, 87 (2017) 61-71.
[41] P.J. Berenson, Film boiling heat transfer from a horizontal surface, J. Heat Transfer, 83 (1961) 351-358.